INTERNATIONAL JOURNAL FOR NUMERICAL METHODS IN FLUIDS, VOL. 9, 405–425 (1989)

A POINT IMPLICIT UNSTRUCTURED GRID SOLVER FOR THE EULER AND NAVIER–STOKES EQUATIONS*

RAJIV R. THAREJA AND JAMES R. STEWART
PRC Kentron, 303 Butler Farm Road, Hampton, VA 23666, U.S.A.

AND

OBEY HASSAN, KEN MORGAN AND JAIME PERAIRE
Institute for Numerical Methods in Engineering, University of Wales, Swansea SA2 8PP, U.K.

SUMMARY

An upwind finite element technique that uses cell-centred quantities and implicit and/or explicit time marching has been developed for computing hypersonic laminar viscous flows using adaptive triangular grids. The approach is an extension to unstructured grids of the LAURA algorithm due to Gnoffo. A structured grid of quadrilaterals is laid out near a solid surface. For inviscid flows the method is stable at Courant numbers of over 100 000. A first-order basic scheme and a higher-order flux-corrected transport (FCT) scheme have been implemented. This technique has been applied to the problem of predicting type III and IV shock wave interactions on a cylinder, with a view to simulating the pressure and heating rate augmentation caused by an impinging shock on the leading edge of a cowl lip of an engine inlet. The predictions of wall pressure and heating rates compare very well with experimental data. The flow features are distinctly captured with a sequence of adaptively generated grids.

KEY WORDS Navier–Stokes equations Euler equations Finite element Hypersonic laminar–viscous flow Time marching Shock wave interactions

INTRODUCTION

Current efforts in the development of hypersonic aircraft have focused a great deal of attention on the design of engine inlets. The forebody of such vehicles is designed to compress the flow through a series of ramps. Shocks emanating from such ramps influence the air flow through the engines and must be accounted for in the analysis because they may produce severe and highly localized heating. Unless specifically designed for such hot-spots, the integrity of the entire vehicle can be jeopardized. Engine designers prefer to coalesce such shock systems on the inlet cowl leading edge to maximize engine performance. Edney[1] has defined a set of six types of shock interference patterns when the bow shock over a cylindrical leading edge is impinged upon by an upstream oblique shock. A type IV interaction produces the most severe heating and is therefore a topic of current research at NASA Langley Research Center.

Experimental studies to date on these phenomena have focused primarily on planar shocks intersecting shock systems generated by three-dimensional bodies or cylinders oriented transverse

---

*Based on a paper originally presented at the AIAA 26th Aerospace Sciences Meeting, Reno, Nevada, January 1988.

0271–2091/89/040405–21$10.50

Received 8 February 1988
Revised 6 June 1988

to the oblique shock (i.e. representative of a wing or tail).[1-4] This has left a void for the designer of two-dimensional engine inlets which would have planar shocks from the inlet compression surfaces intersecting a cylindrical leading edge oriented with its axis parallel to the plane of the shock. In 1971 Craig and Ostwerth[5] experimentally measured pressures and heat transfer rates on a cylindrical leading edge typical of a hypersonic inlet cowl. However, large instrumentation spacing resulted in poor resolution of the peak pressure and heat transfer rates. Recent tests[6,7] performed at the Langely 8-foot High Temperature Tunnel and the Calspan 48-inch Hypersonic Shock Tunnel have produced a set of new experimental data.

Several investigators have attemped analytical solutions of the shock flow field. Edney[1] and Morris and Keyes[8] used oblique shock and Prandtl–Meyer expansion relationships to predict the interference pattern and peak pressure and heat transfer rate with good success. However, their methods rely on experimental measurements of the shock stand-off distance and transmitted shock length. Tannehill and Holst[9] applied a 2D Navier–Stokes finite difference analysis in a simulation of Edney's spherical leading edge results with some success. However, the formulation did not adequately capture the shocks at the high Reynolds numbers of the tests. More recently, White and Rhie[10] used a pressure-based implicit finite volume method, while Klopfer and Yee[11] used a finite volume, total variation diminishing (TVD) scheme to investigate this phenomenon. Their approaches, however, used structured meshes, which require that the spatial discretization be performed in a 'regular' manner, i.e. that each nodal point have the same number of elements around it.

To compute hypersonic flows around arbitrary shapes with complex localized flow phenomena, unstructured grid methods for the Euler equations have been receiving attention recently (e.g. Taylor–Galerkin and Runge–Kutta schemes[12-15]). Work is in progress to extend these approaches to the solution of the Navier–Stokes equations.[16]

Upwind techniques have not been widely employed on unstructured grids to date; a notable exception is the work of Stoufflet *et al.*[17] which uses a vertex scheme and van Leer limiting. In this paper we investigate the implementation of an upwind method in the context of unstructured grids using a cell-centred scheme and flux difference splitting based on the use of Roe's averaging.[18] The work is an unstructured grid implementation of the approach employed in the program LAURA by Gnoffo.[19,20] The adaptive mesh generator[12,21] and this upwind Navier–Stokes solver are combined in a set of programs called LARCNESS, an acronym for Langley adaptive remeshing code and Navier–Stokes solver.

In the next section the development of the inviscid and viscous algorithms is outlined along with the flux-corrected transport (FCT) extension. The main focus—the validation of the analysis by comparison with experimental data and quantitative predictions of shock wave and bow shock interaction on a blunt cylindrical leading edge—is covered in the section on results. A detailed description of the adaptively regenerated meshes is given for a sample case, while results for several incoming shock wave locations are summarized.

SOLUTION ALGORITHM

The solution algorithm employed in this paper is an unstructured grid implementation of a scheme recently presented by Gnoffo.[19,20] The compressible Navier–Stokes equations are written in the conservation form

$$\frac{\partial \mathbf{U}}{\partial t}+\frac{\partial \mathbf{F}^i}{\partial x_i}=\frac{\partial \mathbf{G}^i}{\partial x_i}, \tag{1}$$

where $\mathbf{U}$ is the vector of unknowns and $\mathbf{F}^i$ and $\mathbf{G}^i$ denote the inviscid and viscous fluxes respectively in the direction x_i of a Cartesian co-ordinate system Ox_1x_2. The solution domain Ω is represented by an assembly of triangular and quadrilateral elements. Over a single element Ω_e the integral form of (1) is then

$$\int_{\Omega_e} \frac{\partial \mathbf{U}}{\partial t} \mathrm{d}\Omega = \int_{\Omega_e} \left(\frac{\partial \mathbf{G}^i}{\partial x_i} - \frac{\partial \mathbf{F}^i}{\partial x_i} \right) \mathrm{d}\Omega = \int_{\Gamma_e} n_i (\mathbf{G}^i - \mathbf{F}^i) \, \mathrm{d}\Gamma, \tag{2}$$

where $\mathbf{n}=(n_1,\ n_2)$ denotes the unit outward normal to the boundary Γ_e of Ω_e. Associating unknowns $\mathbf{U}_e$ with each element, this equation may be approximated in the form

$$\Delta \mathbf{U}_e = \mathbf{U}_e^{m+1} - \mathbf{U}_e^m = \frac{\Delta t}{\Omega_e} (\mathrm{IC} + \mathrm{VC}), \tag{3}$$

where $\mathbf{U}_e^m$ denotes the value of $\mathbf{U}_e$ at time $t=t_m$, $\Delta t = t_{m+1} - t_m$ and IC and VC denote the inviscid and viscous contributions respectively to the right-hand side of (2).

Inviscid contributions

The evaluation of the inviscid contributions follows closely the approach described by Gnoffo[19, 20] and full details may be found in his papers. A brief summary is presented here for completeness. The inviscid contributions IC are given by

$$\mathrm{IC} = -\int_{\Gamma_e} n_i \mathbf{F}^i \mathrm{d}\Gamma = -\int_{\Gamma_e} \mathbf{F}_n \, \mathrm{d}\Gamma \tag{4}$$

and are evaluated by summing the contributions from each individual element side Γ_{es} in turn. In this evaluation the normal flux $\mathbf{F}_n$ is replaced by a numerical flux $\tilde{\mathbf{F}}_n$ so that

$$\mathrm{IC} = -\sum_s \int_{\Gamma_{es}} \tilde{\mathbf{F}}_n \, \mathrm{d}\Gamma. \tag{5}$$

For a typical side Γ_{es} with associated elements e and r, Roe's linearization[18] is used to construct the matrix $\mathbf{A}_s$ such that

$$\mathbf{F}_{nr} - \mathbf{F}_{ne} = \mathbf{A}_s(\mathbf{U}_r - \mathbf{U}_e) \tag{6}$$

and the numerical flux is then taken to be

$$\tilde{\mathbf{F}}_n = \tfrac{1}{2}[\mathbf{F}_{ne} + \mathbf{F}_{nr} - |\mathbf{A}_s|(\mathbf{U}_r - \mathbf{U}_e)]. \tag{7}$$

Here it has been assumed that $\mathbf{A}_s$ has been factored as

$$\mathbf{A}_s = \mathbf{R}^{-1} \Lambda \mathbf{R}, \tag{8}$$

where Λ is a diagonal matrix containing the eigenvalues λ_i of $\mathbf{A}_s$ and $|\mathbf{A}_s|$ is defined by

$$|\mathbf{A}_s| = \mathbf{R}^{-1} |\Lambda| \mathbf{R}. \tag{9}$$

The minimum allowable value for λ_i is restricted according to the method proposed by Harten[22] and is such that

$$|\lambda_i| = \begin{cases} |\lambda_i|, & |\lambda_i| > \varepsilon_\lambda, \\ 0{\cdot}5(\lambda_i^2/\varepsilon_\lambda + \varepsilon_\lambda), & |\lambda_i| < \varepsilon_\lambda, \end{cases} \tag{10}$$

where ε_λ is the eigenvalue limiter. For the results presented in this paper the typical value of ε_λ is 0·3. Full details of the entries in the matrices $\mathbf{R}$ and $\mathbf{R}^{-1}$ can be found in the papers by Gnoffo.[19, 20]

We chose to include a structured mesh of several layers of quadrilaterals in the boundary layer region so that we could switch off the value of ε_λ at cell walls parallel to the cylinder to minimize its influence on computed gradients as suggested by Gnoffo.[20] If these inviscid contributions are evaluated at time t_{m+1}, equations (3) leads to the implicit time-stepping scheme

$$\Delta \mathbf{U}_e = -\frac{\Delta t}{\Omega_e}\sum_s \tfrac{1}{2}[\mathbf{F}_{ne}^{m+1} + \mathbf{F}_{nr}^{m+1} - |\mathbf{A}_s^{m+1}|(\mathbf{U}_r^{m+1} - \mathbf{U}_e^{m+1})]\,\delta_s, \qquad (11)$$

where δ_s is the length of the side Γ_{es}.

Linearization of this equation for numerical solution gives

$$\left(\mathbf{I} + \frac{\Delta t}{2\Omega_e}\sum_s |\mathbf{A}_s^*|\delta_s\right)\Delta \mathbf{U}_e = -\frac{\Delta t}{2\Omega_e}\sum_s [\mathbf{F}_{ne}^m + \mathbf{F}_{nr}^* - |\mathbf{A}_s^*|(\mathbf{U}_r^* - \mathbf{U}_e^m)]\delta_s. \qquad (12)$$

Here the linearization has been performed with iterative solution in mind and the superscript* means that the term is evaluated using the latest available solution in the adjacent element. Thus the iterative procedure may be regarded as a point Gauss–Seidel method requiring the inversion of a 4 × 4 matrix for each element in the computational grid. However, with an unstructured grid it is not easy to specify a prescribed direction of sweep through the grid, and the computations reported in this paper have been performed by sweeping through the elements in numbered order in one step and reversing the direction of sweep for the next step. For the unstructured meshes used herein this sweeping is therefore quite random. In this form the algorithm is stable for large values of the Courant number.

In recent papers[12,15] the authors have addressed the problem of the computation of inviscid shock interaction on cylindrical leading edges. In this paper we consider an interaction at a Mach number of 8·03 using the problem definition given in Table I and the computational domain shown in Figure 1. The adaptively regenerated mesh employed 4911 nodes and 9610 triangles as shown in Figure 2. An enlargement of the mesh in the interaction region is also shown. The computed pressure, Mach number and temperature contours are given in Figure 3 to show the global flow phenomena. Enlargements show the flow physics in the region of the interaction and the ability of the technique to resolve these features. The computed and experimentally observed[6,7] pressure distributions over the cylinder surface are in excellent agreement, as shown in Figure 4.

FCT extension

Higher-order accurate evaluations of the numerical flux are not straightforward on unstructured grids, though some successes have been reported.[17,23] Here Zalesak's[24] generalization of the 1D flux-corrected transport (FCT) schemes of Boris and Book[25] is employed with the basic implicit scheme of equation (12). The objective is to limit the diffusion term in (11) so that a $\Delta \mathbf{U}_e$ of

Table I. Description of conditions for viscous shock interaction at $M = 8{\cdot}03$

			Region A	Region B
Reynolds number (inch^{-1})	39774	Mach number	8·03	5·25
Wall temperature (°R)	530	Density (slug ft^{-3})	5·97E-5	1·99E-4
Gas constant (ft^2 s^{-2} °R^{-1})	1716	Velocity (ft s^{-1})	5577·7	5326·9
Gamma	1·4	Flow direction (deg)	0	12·5
Shock angle (deg)	18·1114	Temperature (°R)	200·8	428·4
Prandtl number	0·72			

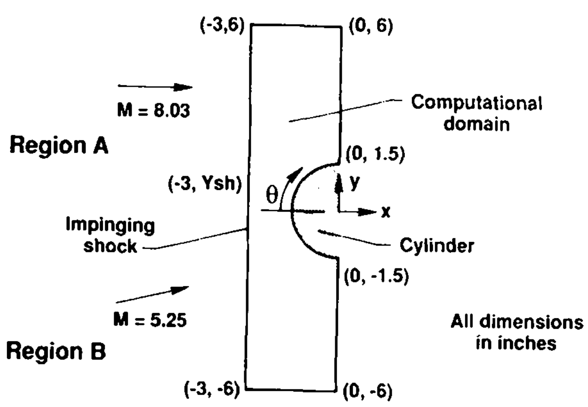

Figure 1. Computational domain for inviscid shock interaction at $M = 8{\cdot}03$.

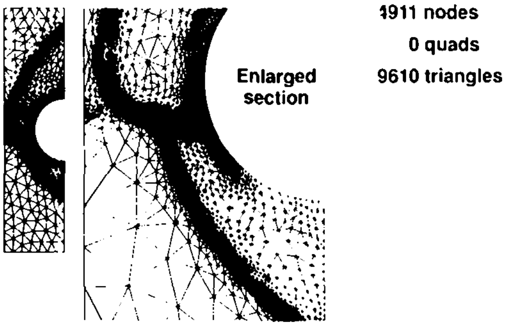

Figure 2. Finite element grid for inviscid shock interaction at $M = 8{\cdot}03$

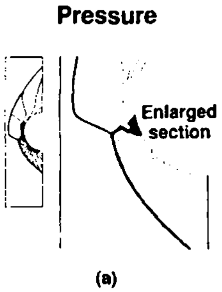

Figure 3(a). Pressure contours for inviscid shock interaction at $M = 8{\cdot}03$

as high an order as possible is produced without introducing overshoots. To ensure conservation, the limiting is performed over the sides and side limiters β_s are determined. The resulting solution is computed according to

$$\left(\mathbf{I}+\frac{\Delta t}{2\Omega_e}\sum_S |\mathbf{A}_s^*|\delta_s\right)\Delta\mathbf{U}_e = -\frac{\Delta t}{2\Omega_e}\sum_S [\mathbf{F}_{ne}^m+\mathbf{F}_{nr}^* - (1-\beta_s)|\mathbf{A}_s^*|(\mathbf{U}_r^*-\mathbf{U}_e^m)]\,\delta_s. \qquad (13)$$

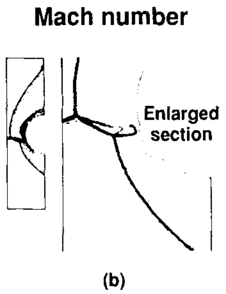

Figure 3(b). Mach number contours for inviscid shock interaction at $M = 8{\cdot}03$

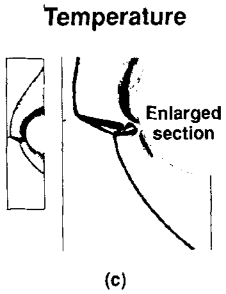

Figure 3(c). Temperature contours for inviscid shock interaction at $M = 8{\cdot}03$

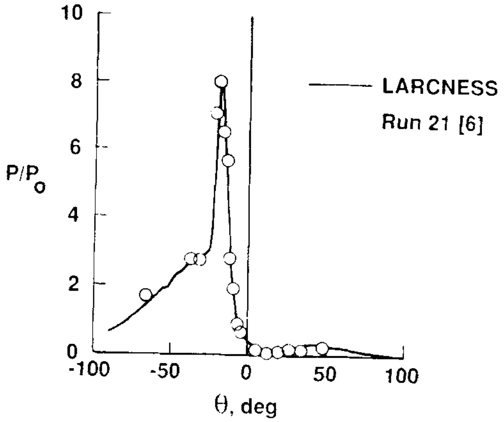

Figure 4. Surface pressure distribution for inviscid shock interaction at $M = 8{\cdot}03$

Viscous contributions

The evaluation of the viscous contributions to the right-hand side of (2) requires a knowledge of the first derivatives of quantities such as the velocity components u_i and the temperature T. The necessary first derivatives have been obtained by a variational recovery process in which the derivatives are represented in a piecewise linear manner over the computational domain; e.g. for the temperature T we can write

$$T=\sum_E T_E P_E, \qquad \frac{\partial T}{\partial x_i}=\sum_I \left.\frac{\partial T}{\partial x_i}\right|_I N_I, \tag{14}$$

where P_E is the piecewise constant shape function associated with element E and N_I is the piecewise linear or bilinear shape function associated with node I,[26] with the nodes placed at the vertices of the elements. The nodal values of the derivatives are obtained from the integral statement

$$\int_\Omega \frac{\partial T}{\partial x_i} N_K \, \mathrm{d}\Omega = \int_\Gamma n_i T N_K \, \mathrm{d}\Gamma - \int_\Omega T \frac{\partial N_K}{\partial x_i} \, \mathrm{d}\Omega \tag{15}$$

by inserting the approximations (14). The result is that

$$\left.\frac{\partial T}{\partial x_i}\right|_K = \frac{1}{(\mathbf{M}_\mathrm{L})_K}\left(\int_\Gamma n_i T N_K \, \mathrm{d}\Gamma - \sum_E \int_{\Omega_E} T_E \frac{\partial N_K}{\partial x_i} \, \mathrm{d}\Omega\right), \tag{16}$$

where the summation appearing in this expression extends only over those elements E which are associated with node K, and $\mathbf{M}_\mathrm{L}$ denotes the standard lumped mass matrix. For a general mesh it is thus possible to write

$$\left.\frac{\partial T}{\partial x_1}\right|_K = T_{x_1 K} - \sum_E \tilde{b}_{KE} T_E, \qquad \left.\frac{\partial T}{\partial x_2}\right|_K = T_{x_2 K} - \sum_E \tilde{c}_{KE} T_E, \tag{17}$$

where $T_{x_1 K}$ and $T_{x_2 K}$ denote the boundary terms and

$$\tilde{b}_{KE} = \frac{1}{(\mathbf{M}_\mathrm{L})_K} \int_{\Omega_E} \frac{\partial N_K}{\partial x_1} \, \mathrm{d}\Omega, \qquad \tilde{c}_{KE} = \frac{1}{(\mathbf{M}_\mathrm{L})_K} \int_{\Omega_E} \frac{\partial N_K}{\partial x_2} \, \mathrm{d}\Omega. \tag{18}$$

Now consider the linearization of the viscous terms for element e. In particular, consider the contribution from a side s which has associated nodes M and N. Then

$$\left.\frac{\partial T}{\partial x_1}\right|_s = \frac{1}{2}\left(T_{x_1 M} - \sum_{E \neq e} \tilde{b}_{ME} T_E - \tilde{b}_{Me} T_e + T_{x_1 N} - \sum_{E \neq e} \tilde{b}_{NE} T_E - \tilde{b}_{Ne} T_e\right) \tag{19}$$

and an evaluation at time $t=t_{m+1}$ can be obtained in the form

$$\left.\frac{\partial T}{\partial x_1}\right|_s^{m+1} = \left.\frac{\partial T}{\partial x_1}\right|_s^{*} - b_{se} \Delta T_e, \tag{20}$$

where

$$b_{se} = \tfrac{1}{2}(\tilde{b}_{Me} + \tilde{b}_{Ne}) \tag{21}$$

and

$$\left.\frac{\partial T}{\partial x_1}\right|_s^{*} = \frac{1}{2}\left(T^*_{x_1 M} + T^*_{x_1 N} - \sum_E \tilde{b}_{ME} T^*_E - \sum_E \tilde{b}_{NE} T^*_E\right). \tag{22}$$

Similarly

$$\left.\frac{\partial T}{\partial x_2}\right|_s^{m+1} = \left.\frac{\partial T}{\partial x_2}\right|_s^{*} - c_{se} \Delta T_e \tag{23}$$

where

$$c_{se} = \tfrac{1}{2}(\tilde{c}_{Me} + \tilde{c}_{Ne}). \tag{24}$$

The corresponding expressions for the gradients of the velocity components may now be written directly. The inclusion of the viscous contributions changes (12) to read

$$\left(\mathbf{I}+\frac{\Delta t}{\Omega_e}\sum_s(\tfrac{1}{2}|\mathbf{A}_s^*|-\mathbf{B}_s)\delta_s\right)\Delta\mathbf{U}_e=-\frac{\Delta t}{\Omega_e}\sum_s\{\tfrac{1}{2}[\mathbf{F}_{ne}^m+\mathbf{F}_{nr}^*-|\mathbf{A}_s^*|(\mathbf{U}_r^*-\mathbf{U}_e^m)]-\mathbf{G}_{ns}^*\}\delta_s, \tag{25}$$

where $\mathbf{G}_{ns}^*$ denotes the viscous contribution obtained using the latest available values. The entries B_{ij} in the matrix $\mathbf{B}_s$ can be obtained by inserting expressions such as (20) and (23) into the viscous fluxes and expressing the increments Δu_i and ΔT in terms of the increments in the conserved variables. The result is that

$$\begin{aligned}
&B_{11}=B_{12}=B_{13}=B_{14}=0, \qquad B_{21}=(\phi_{1s}u_{1e}^m+\phi_{2s}u_{2e}^m)/\rho_e^m,\\
&B_{22}=-\phi_{1s}/\rho_e^m, \qquad B_{23}=-\phi_{2s}/\rho_e^m, \qquad B_{24}=0,\\
&B_{31}=(\phi_{3s}u_{1e}^m+\phi_{4s}u_{2e}^m)/\rho_e^m, \qquad B_{32}=-\phi_{3s}/\rho_e^m, \qquad B_{33}=-\phi_{4s}/\rho_e^m,\\
&B_{34}=0, \qquad B_{41}=-\gamma\phi_{7s}[(u_{1e}^2+u_{2e}^2)^m-(\rho\varepsilon)_e^m]/(\rho_e^m)^2+u_{1e}^m\phi_{5s}/\rho_e^m+u_{2e}^m\phi_{6s}/\rho_e^m,\\
&B_{42}=-\phi_{5s}/\rho_e^m+\gamma\phi_{7s}u_{1s}^m/\rho_e^m, \qquad B_{43}=-\phi_{6s}/\rho_e^m+\gamma\phi_{7s}u_{2e}^m/\rho_e^m, \quad B_{44}=-\gamma\phi_{7s}/\rho_e^m,
\end{aligned} \tag{26}$$

where

$$\begin{aligned}
&\phi_{1s}=\alpha(4n_1b_{se}/3+n_2c_{se}), \qquad \phi_{2s}=\alpha(-2n_1c_{se}/3+n_2b_{se}),\\
&\phi_{3s}=\alpha(n_1c_{se}-2n_2b_{se}/3), \qquad \phi_{4s}=\alpha(n_1b_{se}+4n_2c_{se}/3),\\
&\phi_{5s}=(u_{1s}\phi_{1s}+u_{2s}\phi_{3s}), \qquad \phi_{6s}=\alpha(u_{1s}\phi_{2s}+u_{2s}\phi_{4s}),\\
&\phi_{7s}=\alpha(n_1b_{se}+n_2c_{se})/Pr
\end{aligned} \tag{27}$$

and

$$\alpha=\mu_s/Re. \tag{28}$$

In these expressions *Re* and *Pr* denote the Reynolds and Prandtl numbers respectively.

The complexity of the evaluation of the viscous contribution $\mathbf{G}_{ns}^*$ in (25) is such that in the current implementation it has been replaced by $\mathbf{G}_{ns}^m$. Thus the iterative solution algorithm is effectively point Gauss–Seidel for the inviscid contributions and point Jacobi for the viscous contributions. This probably has the effect of lowering the maximum Courant number that can be used. Compared to inviscid flows where very large Courant numbers can be run, the maximum permissible Courant number for viscous analyses is about 5–10 on highly stretched meshes.

SHOCK INTERACTION RESULTS

Recently, tests were performed in the Calspan 48-inch Hypersonic Shock Tunnel (48″ HST) to study the interaction of an impinging shock with a bow shock on a cylinder.[6–8] This tunnel is started by rupturing a double diaphragm which permits high-pressure gas in the driver section to expand into the driven section, and in so doing generates a normal shock which propagates through the low-pressure air. A region of high-temperature, high-pressure air is produced between this normal shock front and the gas interface between the driver and driven gas, often referred to as the contact surface. When the primary or incident shock strikes the end of the driven section it is reflected, leaving a region of almost stationary high-pressure heated air. This air is then expanded through a contoured nozzle to the test section. The typical test time is about

10 ms. The tests were run at Mach numbers of 6·3 and 8·0, total temperatures ranging from 2100 to 3040°R and freestream unit Reynolds numbers of $0{\cdot}7\times10^6$ to $4{\cdot}9\times10^6$ per foot.

Continued evaluation of these data after initial publications[6, 7] has shown the interaction to be unsteady and the gauge temperatures to be significantly higher than the temperature of the stainless steel model. The data reduction technique developed by Rae and Tauber used in the reduction of the test results in the Langley 8-foot High Temperature Tunnel[6] has been employed in the reduction of the Calspan 48" HST data. This technique, based on a closed form solution for a semi-infinite slab with temperature-dependent properties,[27] treats the heat flux as a series of step impulses rather than a constant and hence better accounts for the time transient heat flux caused by the motion of the shock interference pattern. Implementation has shown the Mach 8 data to be significantly higher than previously reported. The data herein are compared with the latest unpublished data (obtained from Allan R. Wieting and Michael S. Holden) which are uncorrected for wall temperature. The experimental value of stagnation heating rate for the undisturbed cylinder at $M=8{\cdot}03$ (run 21) was 61·7 Btu/ft^2 s. A three-dimensional viscous shock layer (VSL)[28] analysis (corrected for 2D by a factor 0·74312) of this run with a perfect gas analysis for laminar flow conditions predicted a rate of 41·43 Btu/ft^2 s. A 2D Fay and Riddell solution predicted 45·52 Btu/ft^2 s which compares well with VSL. The differences between the experimental and analytical values have not been resolved, but could result from high-temperature effects not accounted for or high free stream turbulence levels. This difference has been factored out of our results by normalizing the experimental heating rates by the experimental undisturbed stagnation value (61·7), while our predictions have been normalized by the viscous shock layer value (41·43).

Computationally, in order to simulate shock impingment onto the cowl lip of an engine inlet, a spectrum of cases with different shock locations was computed. The computational domain was a rectangular region enveloping the cylinder as shown in Figure 5. Inflow conditions in the free stream region (denoted as region A and B) are given in Table I. Experimentally, the impinging shock was generated by an upstream wedge which deflected the flow in region B upward by 12·5°. The conditions behind this impinging shock are also given in Table I. The vertical location Y_{sh} (see Table II for the notation of these cases) of the intersection of the impinging shock with the computational domain was varied to generate eight different cases (S1–S8) which generated type III and IV interference patterns. In order to best capture the location of the peak in the experimental heating rate, another shock location (denoted as case SO) was selected based on a linear interpolation of the locations of the peaks in computed heating rates in cases S1–S8 and the location of the peak heating rate in the experiment.

A typical computation is described for the three meshes used to obtain solutions for flow corresponding to case S0. For all three meshes an unstructured grid consisting only of triangles

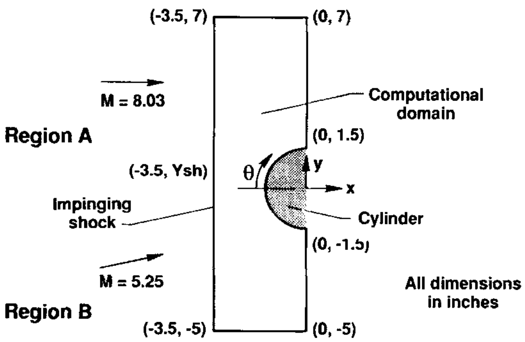

Figure 5. Computational domain for viscous shock interaction at $M=8{\cdot}03$

Table II. Shock locations for viscous shock interaction at $M=8{\cdot}03$

CASE	Y_{sh} (inch)
S1	−0·2635353
S2	−0·3635353
S3	−0·4635353
S0	−0·5226670
S4	−0·5635353
S5	−0·6635353
S6	−0·7635353
S7	−0·8635353
S8	−0·9635353

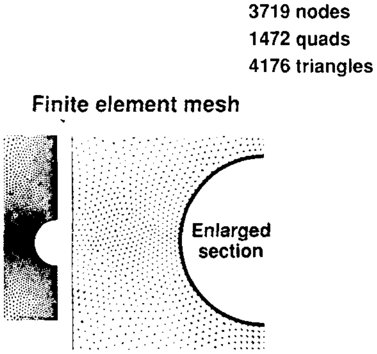

Figure 6(a). Finite element mesh 1

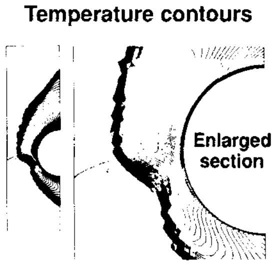

Figure 6(b). Temperature contours

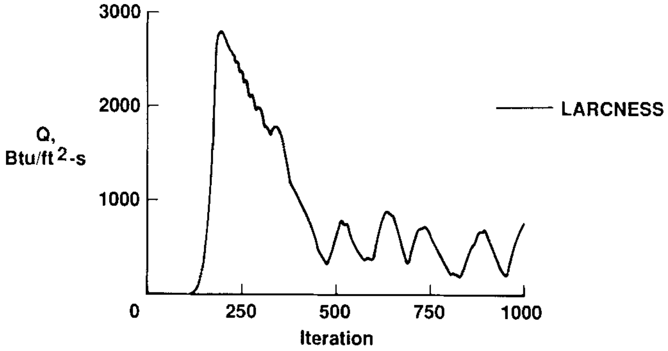

Figure 6(c). Maximum surface heating rate versus iteration

was generated in the entire computational domain except in the vicinity of the cylinder. In this region 32 layers of stretched structured quadrilaterals were generated with the circumferential distribution dictated by the unstructured mesh. The thickness of the first layer was 1×10^{-5} inch and an expansion ratio of 1·24 was used for the subsequent layers. Unless otherwise mentioned the runs were made with a Courant number of 3.

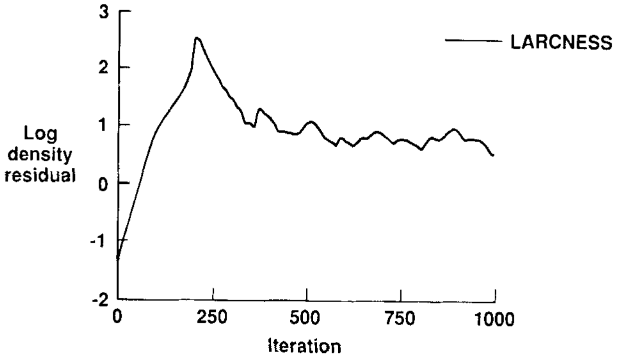

Figure 6(d). Density residual versus iteration

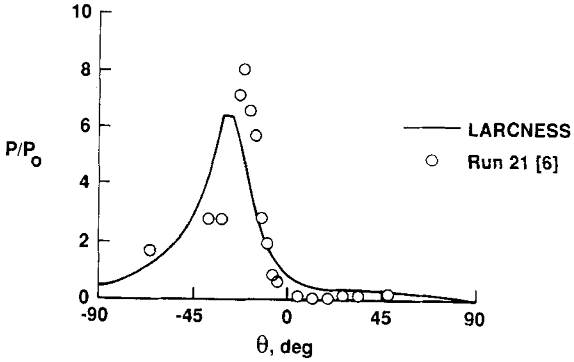

Figure 6(e). Surface pressure distribution

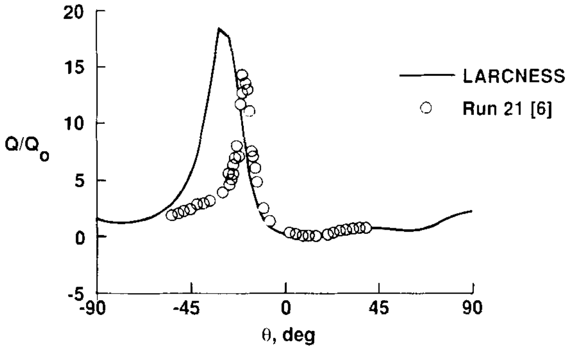

Figure 6(f). Surface heating rate distribution

An initial almost uniform mesh (mesh 1) consisted of 4176 triangular elements in the unstructured region and an additional 1472 quadrilaterals along the cylinder. The mesh and temperature contours for this computation are shown in Figures 6(a) and 6(b) respectively along with an enlarged section of the same. This coarse grid was adequate to get the essential features of the problem. The Courant number was increased from 0·3 to 3·0 in 200 iterations and then held

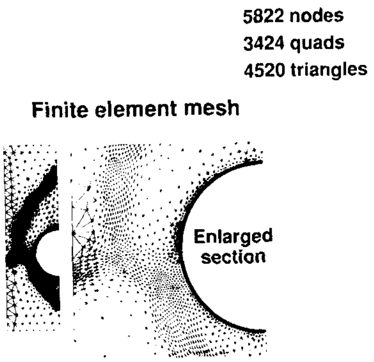

Figure 7(a). Finite element mesh 2

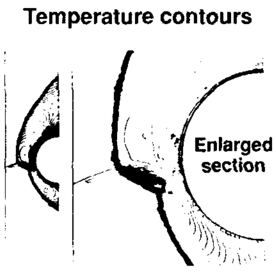

Figure 7(b). Temperature contours

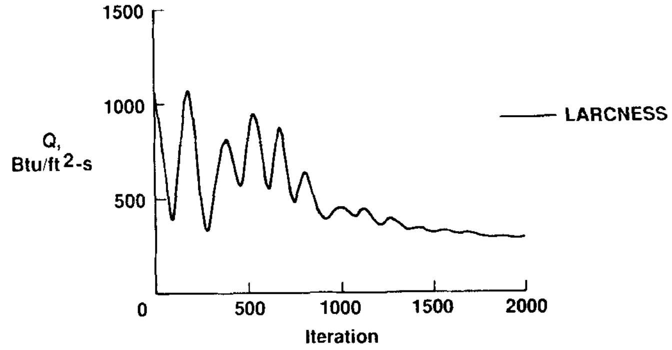

Figure 7(c). Maximum surface heating rate versus iteration

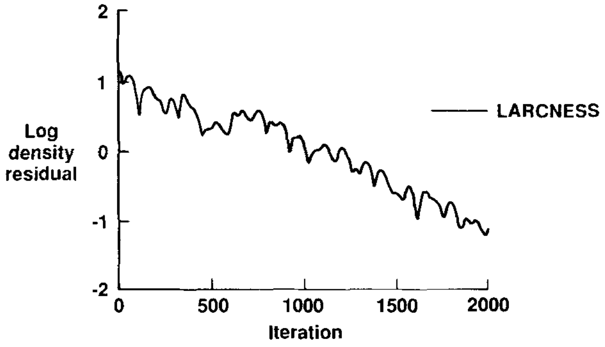

Figure 7(d). Density residual versus iteration

constant at 3·0. For this mesh 1000 iterations were performed using the basic or non-FCT scheme. The maximum value of heat transfer rate on the cylinder as a function of iteration number is shown in Figure 6(c). Due to the coarseness of the mesh the location of the maximum value of heating rate oscillated after about 500 iterations. This is also evident in the residual behaviour (Figure 6(d)). The wall distributions of the pressure and heating rate normalized by the undisturbed values are compared with experiment in Figures 6(e) and 6(f) respectively. These

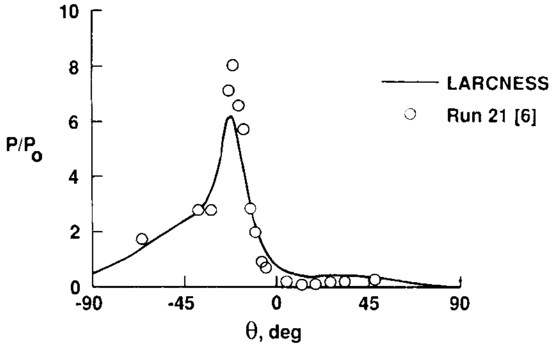

Figure 7(e). Surface pressure distribution

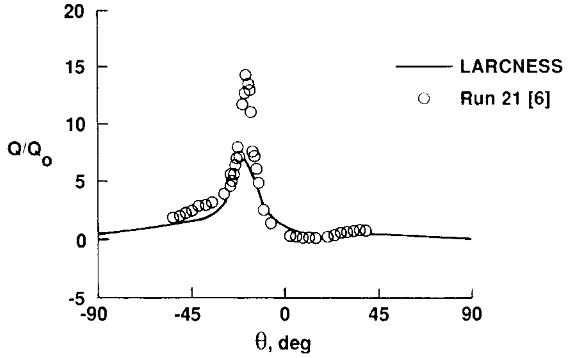

Figure 7(f). Surface heating rate distribution

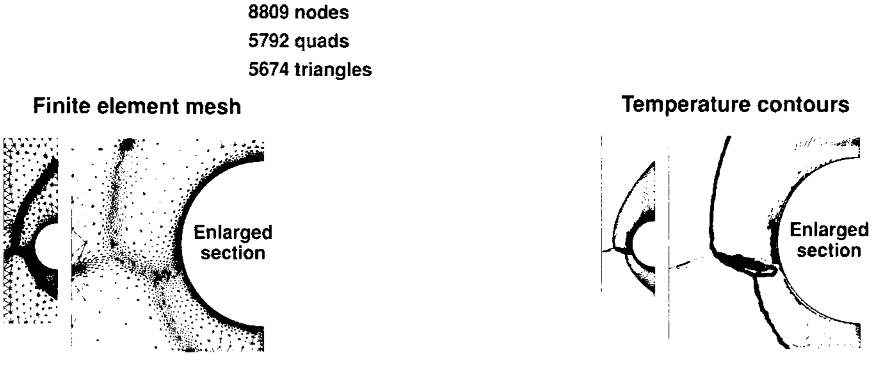

Figure 8(a). Finite element mesh 3

Figure 8(b). Temperature contours

surface results show the augmentation above the undisturbed values at the interaction point on the surface.

From the solution on this initial mesh, and using a combination of the gradients of density and Mach number as error indicators for the remeshing, a second mesh was generated. This mesh consisted of 4520 triangles and 3424 quadrilaterals in the structured region. A total of 2000 iterations were performed on this intermediate mesh. See Figures 7(a) and 7(b) for the mesh and

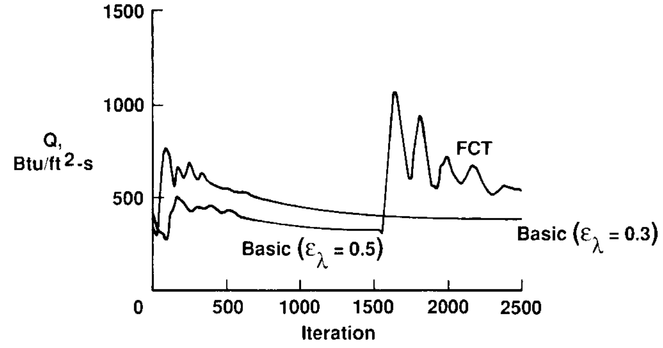

Figure 8(c). Maximum surface heating rate versus iteration

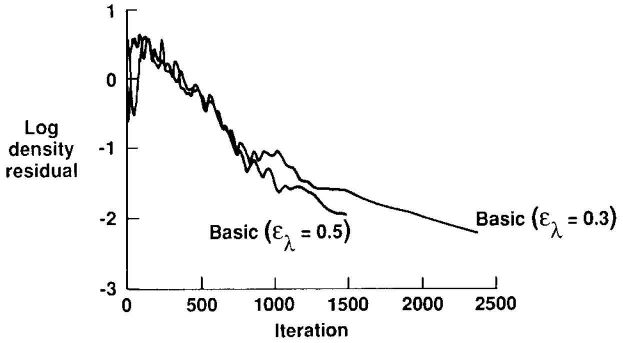

Figure 8(d). Density residual versus iteration

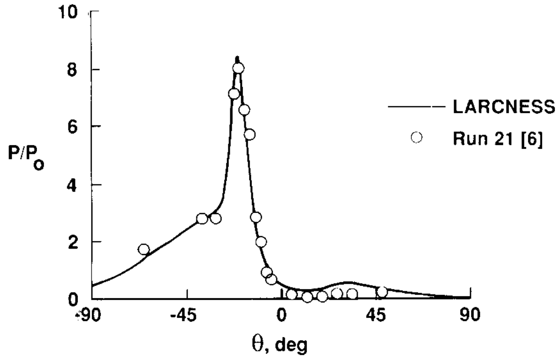

Figure 8(e). Surface pressure distribution

temperature contours. The maximum heating rate converged after about 1500 iterations as shown in Figure 7(c), while the density residual decreased by two orders of magnitude (Figure 7(d)). The heating rate and pressure distributions were below the experimental values (Figures 7(e) and 7(f)), but have shifted in circumferential position and sharpened.

A third mesh was generated in a similar fashion. This mesh consisted of 5674 triangles and 5792 quadrilaterals (Figure 8(a) and 8(b)). The temperature contours show most of the significant flow

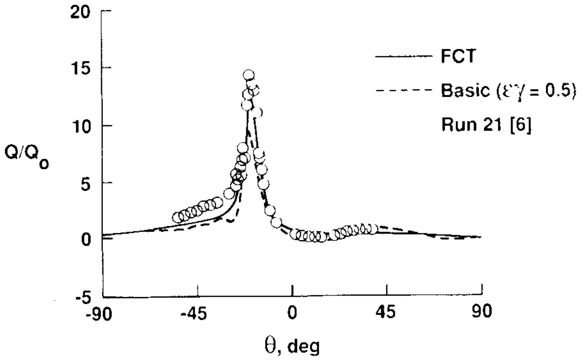

Figure 8(f). Surface heating rate distribution

features for this type IV interaction and are clearly showing more details of the flow phenomena. However, since this solution was obtained with the basic scheme, some smearing is evident. The maximum value of heating rate on the cylinder for values of the eigenvalue limiter (see Equation (10)) $\varepsilon_\lambda = 0{\cdot}5$ and 0·3 is shown in Figure 8(c). The lower value of 0·3 gave a heating rate which was slightly higher, as expected due to lower dissipation. The solution from $\varepsilon_\lambda = 0{\cdot}5$ was restarted after 1500 iterations using the FCT scheme. After about 1000 iterations convergence was achieved. The residual behaviour for this case is shown in Figure 8(d). Gnoffo[19,20] mentions that it is necessary to close out a computation for his higher-order scheme by reducing the Courant number to 0·3 for a few hundred iterations in order to bring down the residual. In our computations the Courant number was gradually lowered from 3 to 1. As in Gnoffo's scheme for this FCT approach, convergence was degraded, while the basic scheme was seen to converge. For these reasons convergence in the FCT scheme was based on convergence of the value of the maximum heating rate. The wall distributions of the pressure and heating rates compare quite well with experiment (Figures 8(e) and 8(f)). The experimental heating rate was higher than computed in the region $\theta = -50°$ to $-30°$, possibly due to turbulence. Figure 9 shows the contours of several flow quantities obtained with FCT.

Figure 10 compares the temperature contours obtained with FCT with the basic scheme for the eight shock locations computed (cases S1–S8). Significantly sharper features of the flow are captured. The sensitivity of the flow to slight variations in the inflow shock location is evident in this series of solutions. In each successive case the impinging shock is moved down by 0·1 inch. The first several cases are clearly a type IV interaction, while the last few are of type III. Table III shows the effect of FCT on the peak values and locations of pressure and heating rates compared to the basic scheme with the eigenvalue limiter $\varepsilon_\lambda = 0{\cdot}5$. Earlier predictions showed an amplification of about 8 and 9·5 in the pressure and heating rates compared to the undisturbed case.[6] However, our FCT solutions indicate that these values are higher, about 9·53 and 14·23 respectively. Note that the peak occurs at $\theta = -19{\cdot}00°$ for the experiment and $\theta = -19{\cdot}08°$ for the analysis. As stated earlier, improved data reduction techniques indicate that the peak heat transfer amplification is 14·28 at a wall temperature of 1023 °R. The previously reported peak was 9·52.[16] Adjusting this value for a wall temperature of 530 °R by ratioing the driving enthalpy differences across the stagnation point thermal layer would increase this value to 18·26. It should be pointed out that our analysis assumes a perfect gas and laminar flow conditions, while the test might have significant real gas effects and turbulence. Inspite of these differences, we feel that the current laminar version of the LARCNESS program does a remarkably good job of predicting the flow phenomena and

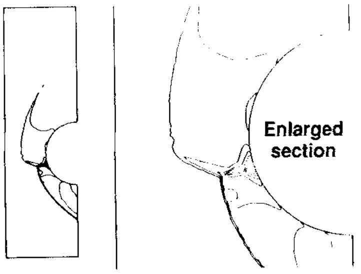

Figure 9(a). Density contours for viscous shock interaction at $M = 8{\cdot}03$ (case S0, mesh 3, FCT scheme)

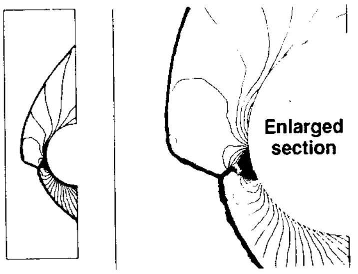

Figure 9(b). Pressure contours for viscous shock interaction at $M = 8{\cdot}03$ (case S0, Mesh 3, FCT scheme)

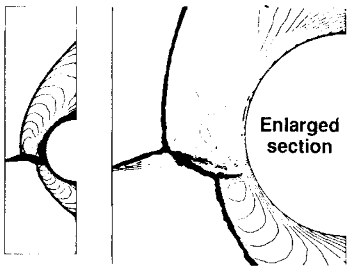

Figure 9(c). Mach number contours for viscous shock interaction at $M = 8{\cdot}03$ (case S0, mesh 3, FCT scheme)

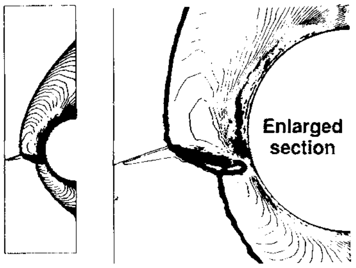

Figure 9(d). Temperature contours for viscous shock interaction at $M = 8{\cdot}03$ (case S0, mesh 3, FCT scheme)

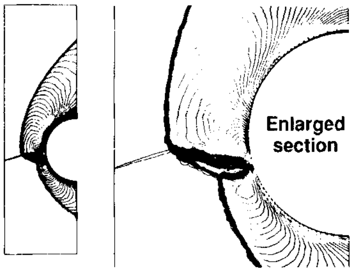

Figure 9(e). U-velocity contours for viscous shock interaction at $M = 8{\cdot}03$ (case S0, mesh 3, FCT scheme)

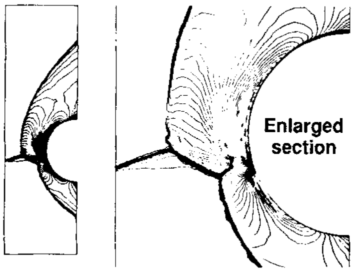

Figure 9(f). V-velocity contours for viscous shock interaction at $M = 8{\cdot}03$ (case S0, mesh 3, FCT scheme)

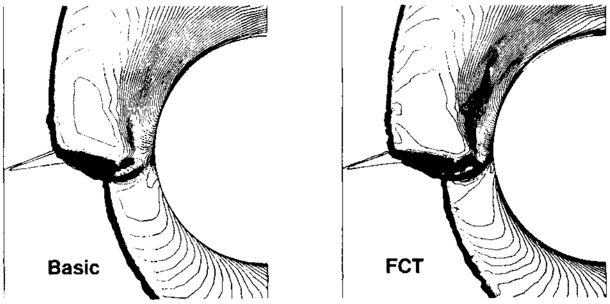

Figure 10(a). Comparison of temperature contours for basic and FCT schemes for viscous shock interaction at $M = 8{\cdot}03$ (case S1, mesh 3)

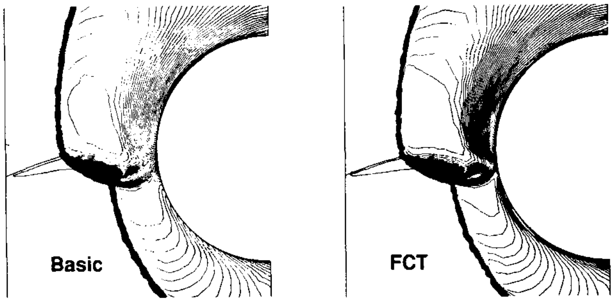

Figure 10(b). Comparison of temperature contours for basic and FCT schemes for viscous shock interaction at $M = 8{\cdot}03$ (case S2, mesh 3)

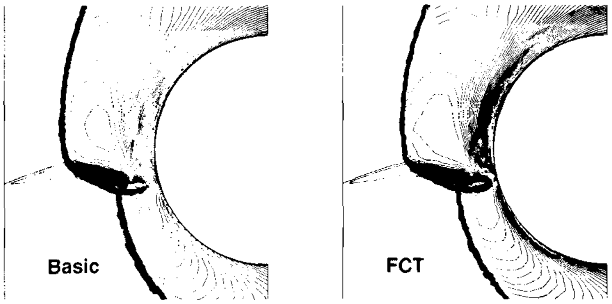

Figure 10(c). Comparison of temperature contours for basic and FCT schemes for viscous shock interaction at $M = 8{\cdot}03$ (case S3, mesh 3)

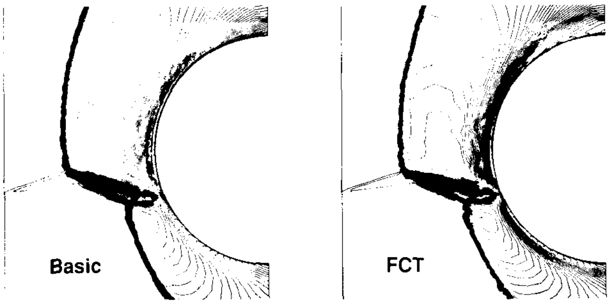

Figure 10(d). Comparison of temperature contours for basic and FCT schemes for viscous shock interaction at $M = 8{\cdot}03$ (case S4, mesh 3)

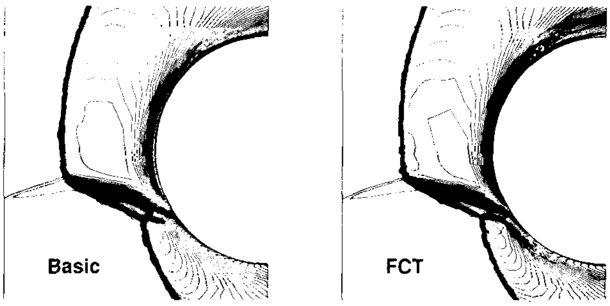

Figure 10(e). Comparison of temperature contours for basic and FCT schemes for viscous shock interaction at $M = 8{\cdot}03$ (case S5, mesh 3)

wall pressures and heating rates. For the basic and FCT schemes the peak values of pressure and heat transfer rate versus the circumferential location of the cylinder for all cases S1–S8 and S0 are shown in Figures 11 and 12 to illustrate the sensitivity of peak locations of pressure and heating rates respectively to the shock impingement location and the effect of using the FCT scheme rather than the basic scheme.

CONCLUSIONS

An upwind finite element technique that uses cell centred quantities and implicit and/or explicit time marching has been developed for computing hypersonic laminar viscous flows using

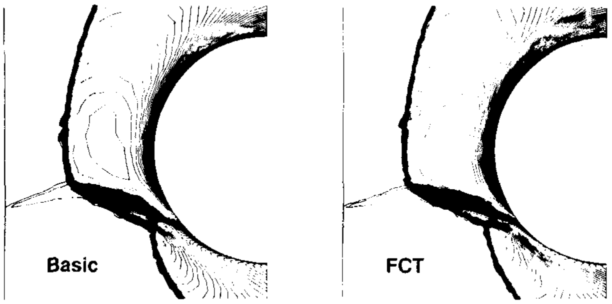

Figure 10(f). Comparison of temperature contours for basic and FCT schemes for viscous shock interaction at $M = 8{\cdot}03$ (case S6, mesh 3)

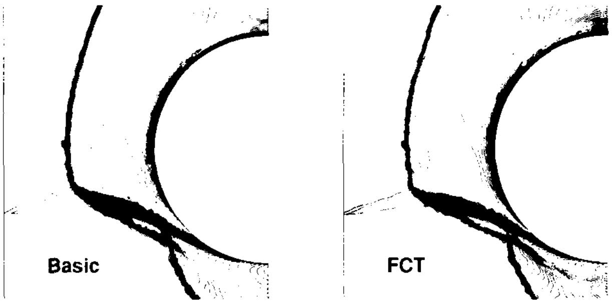

Figure 10(g). Comparison of temperature contours for basic and FCT schemes for viscous shock interaction at $M = 8{\cdot}03$ (case S7, mesh 3)

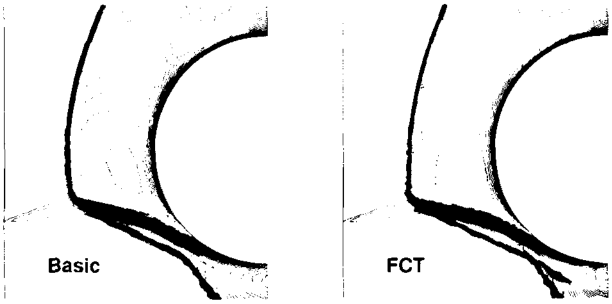

Figure 10(h). Comparison of temperature contours for basic and FCT schemes for viscous shock interaction at $M = 8{\cdot}03$ (case S8, mesh 3)

unstructured triangular grids. A structured grid of quadrilaterals is laid out near a solid surface. For inviscid flows the method is stable at Courant numbers of over 100 000. For viscous flows on highly stretched meshes the method is stable for Courant numbers of around 5–10. A first-order basic scheme and a flux-corrected transport (FCT) scheme have been implemented. This technique has been applied to the problem of predicting type III and IV shockwave interactions on a cylinder, with a view to simulating the pressure and heating rate augmentation caused by an impinging shock on the leading edge of a cowl lip of an engine inlet. The predictions of wall pressure and heating rates compare very well with other computational schemes (e.g. viscous shock layer and Fay and Riddell) and experimental data. The flow features are distinctly captured with a sequence of adaptively generated grids.

Table III. Peak amplifications and locations for basic and FCT schemes for viscous shock interaction at $M = 8{\cdot}03$

Case	P/P_0 Basic	P/P_0 FCT	θ (deg) FCT	Q/Q_0 Basic	Q/Q_0 FCT	θ (deg) FCT
S1	5·04	5·43	−5·53	5·00	6·20	−5·53
S2	5·57	6·27	−10·32	5·76	8·20	−10·32
S3	6·57	8·56	−15·05	7·02	12·73	−15·05
S0	7·31	9·33	−19·08	7·96	13·09	−19·08
S4	7·40	9·53	−22·62	8·17	14·23	−21·73
S5	6·75	8·73	−34·15	7·58	12·52	−34·15
S6	5·53	7·49	−37·02	5·31	11·41	−37·02
S7	4·02	4·70	−47·47	3·33	5·47	−48·47
S8	2·98	3·03	−50·51	2·18	2·74	−52·49

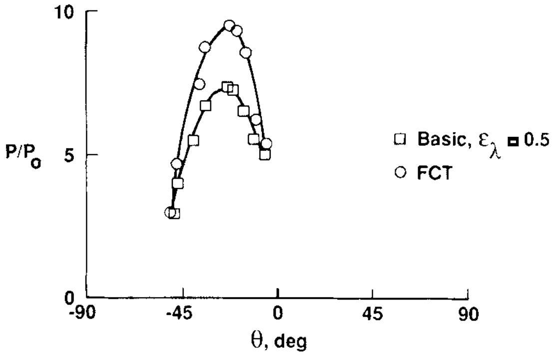

Figure 11. Surface pressure amplification for basic and FCT schemes for viscous shock interaction at $M = 8{\cdot}03$ (case S1–S8, mesh 3)

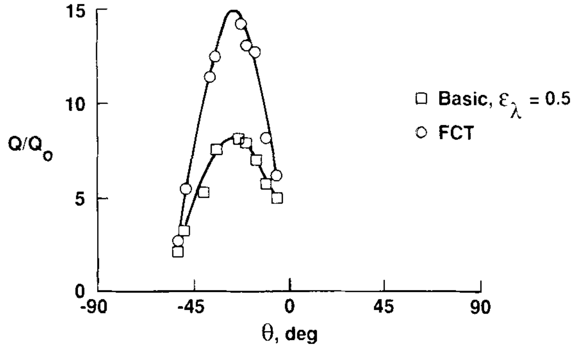

Figure 12. Surface heating rate amplification for basic and FCT schemes for viscous shock interaction at $M = 8{\cdot}03$ (case S1–S8, mesh 3)

Our first experiences with this method appear quite promising. However, a wider class of flow problems needs to be computed in order to assess fully its adequacy for solving viscous hypersonic flows. Work is currently in progress to extend this approach to more realistic and challenging 3D configurations.

ACKNOWLEDGEMENTS

The authors would like to thank Dr. Allan Wieting, Head, Aerothermal Loads Branch, Loads and Aeroelasticity Division, NASA Langley Research Center for many valuable discussions and a grant (NAGW-478) that supported this research. The authors also wish to express their thanks to Dr. Peter Gnoffo, Aerothermodynamics Branch, Space Systems Division, NASA Langley Research Center for many informative discussions during the course of this work.

REFERENCES

1. B. Edney, 'Anomalous heat transfer and pressure distributions on blunt bodies at hypersonic speeds in the presence of an impinging shock', *FFA Report 115*, Aero. Res. Inst. of Sweden, 1968.
2. B. M.Ryan, 'Summary of the aerothermodynamic interference literature', *Technical Note 4061-160*, Naval Weapons Center, 1969.
3. R. H. Korkegi, 'Survey of viscous interactions associated with high Mach number flight', *AIAA J.*, **9**, (1971).
4. J. W. Keyes and F. D. Haines, 'Analytical and experimental studies of shock interference heating in hypersonic flow', *NASA TN D-7139*, 1973.
5. R. R. Craig and P. J. Ostwerth, 'Experimental study of shock impingement on a blunt leading edge with application to hypersonic engine inlet design', *AFAPL-TR-71-10*, 1971.
6. A. R. Wieting, 'Experimental study of shock wave interference heating on a cylindrical leading edge', *Ph.D. dissertation*, Old Dominion University, Norfolk, Virginia, 1987; also *NASA TM-100484*, 1987.
7. A. R. Wieting and M. S. Holden, 'Experimental study of shock wave interference heating on a cylindrical leading edge', *AIAA Paper 87-1511*, 1987.
8. D. K. Morris and J. W. Keyes, 'Computer programs predicting supersonic and hypersonic interference flow fields and heating', *NASA TM X-2725*, 1973.
9. J. C. Tannehill and T. L. Hoist, 'Numerical computation of two-dimensional viscous blunt body flows with an impinging shock', *AIAA J.*, **14**, (1976).
10. J. A. White and C. M. Rhie, 'Numerical analysis of peak heat transfer rates for hypersonic flow over a cowl leading edge', *AIAA Paper 87-1895*, 1987.
11. G. H. Klopfer and H. C. Yee, 'Viscous hypersonic shock on shock interaction on blunt cowl lips', *AIAA Paper 88-0233*, 1988.
12. K. Morgan, J. Peraire, R. R. Thareja and J. R. Stewart, 'An adaptive finite element scheme for the Euler and Navier–Stokes equations', *AIAA Paper 87-1172-CP*, 1987.
13. R. Shapiro and E. M. Murman, 'Cartesian grid finite element solutions to the Euler equations', *AIAA Paper 87-0555*, 1987.
14. R. Ramakrishnan, K. S. Bey and E. A. Thornton, 'An adaptive quadrilateral and triangular finite element scheme for compressible flows', *AIAA Paper 88-0033*, 1988.
15. J. R. Stewart, R. R. Thareja, A. R. Wieting and K. Morgan, 'Inviscid finite element validation of shock interference on a cylindrical leading edge', *AIAA Paper 88-0368*, 1988.
16. O. Hassan, 'Taylor Galerkin finite element solutions of the Navier–Stokes equations', *Ph.D. dissertation*, University of Wales, Swansea, 1988.
17. B. Stoufflet, J. Peraire, F. Fezoui and A. Dervieux, 'Numerical simulation of 3D hypersonic Euler flows around space vehicles using adapted finite elements', *AIAA Paper 87-0560*, 1987.
18. P. L. Roe, 'Approximate Riemann solvers, parameter vectors and difference scheme', *Comput. Phys.*, **43**, 357–372 (1981).
19. P. A. Gnoffo, 'Application of program Laura to three-dimensional AOTV flowfields', *AIAA Paper 86-0565*, 1986.
20. P. A. Gnoffo and R. S. McCandless, 'Enhancements to program Laura for computation of three-dimensional hypersonic flow', *AIAA Paper 87-0280*, 1987.
21. J. Peraire, M. Vahdati, K. Morgan and O. C. Zienkiewcz, 'Adaptive remeshing for compressible flow computations', *Comput. Phys.* **72**, 449–466 (1987).
22. A. Harten, 'High resolution schemes for hypersonic conservation laws', *DOE/ER/03077-175*, Courant Mathematics and Computing Laboratory, NYU, 1982.
23. R. Löhner, K. Morgan, J. Peraire and M. Vahdati, 'Finite element flux corrected transport for the Euler and Navier–Stokes equations', *Int. numer. methods fluids*, **7**, 1093–1109 (1987).
24. S. T. Zalesak, 'Fully multidimensional flux corrected transport algorithm for fluids', *Comput. Phys.*, **31**, 335–362 (1979).
25. J. P. Boris and D. L. Book, 'Flux corrected transport I: SHASTA, a transport algorithm that works', *J. Comput. Phys.* **11**, 38–69 (1973).
26. O. C. Zienkiewicz and K. Morgan, *Finite Elements and Approximation*, Wiley, New York, 1983.
27. H. S. Carslaw and J. C. Jaeger, *Conduction of Heat in Solids*, 2nd Edn, Clarendon Press, 1959.
28. R. R. Thareja, K. Y. Szema and C. H. Lewis, 'Effects of chemical equilibrium on three-dimensional viscous shock layer analysis of hypersonic laminar or turbulent flows', *AIAA Paper 82-0305*, 1982.